Moving-target tracking in single-channel wide-beam SAR

Henke, Daniel ; Magnard, Christophe ; Frioud, Max ; Small, David ; Meier, Erich ; Schaepman, Michael E

Abstract: A novel method for moving-target tracking using single-channel synthetic aperture radar (SAR) with a large antenna beamwidth is introduced and evaluated using a field experiment and real SAR data. The presented approach is based on subaperture SAR processing, image statistics, and multitarget unscented Kalman filtering. The method is capable of robustly detecting and tracking moving objects over time, providing information not only about the existence of moving targets but also about their trajectories in the image space while illuminated by the radar beam. We have successfully applied the method on an experimental data set using miniature SAR to accurately characterize the movement of vehicles on a highway section in the radar image space.

DOI: https://doi.org/10.1109/tgrs.2012.2191561

Moving target tracking in single-channel, wide-beam SAR

Daniel Henke, Christophe Magnard, Max Frioud, David Small, *Member, IEEE,* Erich Meier, and Michael E. Schaepman, *Senior Member, IEEE*

***Abstract*—A novel method for moving target tracking using single-channel Synthetic Aperture Radar (SAR) with a large antenna beam width is introduced and evaluated using a field experiment and real SAR data. The presented approach is based on sub-aperture SAR processing, image statistics and multitarget unscented Kalman filtering. The method is capable of robustly detecting and tracking moving objects over time, providing information not only about the existence of moving targets but additionally about their trajectories in the image space while illuminated by the radar beam. We have successfully applied the method on an experimental data set using MiSAR to accurately characterize the movement of vehicles on a highway section in the radar image space.**

***Index Terms*—Kalman filtering, Tracking, Tracking filters, Synthetic Aperture Radar.**

I. Introduction

TRACKING MOVING objects in SAR data is a challenging task demanding state-of-the-art processing. Traditional moving target indication (MTI) in SAR data relies on space-time adaptive processing [1],[2] along-track interferometry [3],[4], displaced phase centre array [5], detection by focusing with different estimated velocity vectors [6], monopulse processing [7], exploiting patch differences in autofocus results [8] or a combination of the above [9], [10]. An alternative approach for MTI solutions is the development of new sensor technologies, e.g. a special MTI mode as the scan-MTI mode of PAMIR [11],[12],[13]. However, for some of these approaches the restrictions on the movements of the object, e.g. only linear motion, and on the transmitter flight track limit the potential applications. Furthermore, in most methodologies, multiple antenna channels are required to achieve satisfactory detection probability and the presence of moving objects is only indicated with limited information about the speed and direction of detected objects. However, when dealing with ultra-lightweight sensors such as MiSAR ([14],[15]) – commonly required in unmanned aerial vehicles (UAVs) – generation of multi-channel data may not be feasible. Therefore, to overcome these problems, we make use of an approach based on image statistics of geocoded SAR images, unscented Kalman filtering and multi-target hypotheses to extract the movement of objects illuminated by the beam of a suitable single-channel, wide-beam SAR sensor. We propose a combination of image processing and advanced multi-target tracking techniques with hidden state space representation as a promising approach for solving the problem of multiple targets with movements that contain a certain degree of non-uniformity and non-linearity, to overcome the above listed limitations. Multi-target tracking for radar applications is presented in [16]. Special emphasis has been placed on improving existing tracking methods in recent years within the computer science community, with applications to a variety of problems [17], [18], [19]. These promising approaches are introduced and adapted to the tracking of moving objects in SAR data [20] where a general framework is demonstrated.

Based on above progress, an algorithm to track moving objects in wide-beam, single-channel systems was developed and evaluated. The proposed algorithm which relies on the processing of a large number of highly "Overlapping Apertures with reduced Bandwidth" (OAwrB) and subsequent tracking of anomalies in the temporal image statistics provides a flexible and promising solution for the tracking of moving objects even under conditions where most other methods available for single-channel SAR systems fail. We demonstrate that by successfully testing the method on a data set recorded with the wide-beam, single-channel MiSAR system in southern Germany, where we were able to accurately extract the trajectories of most of the cars and trucks on a highway and its associate on-ramps in the *image* space. However, these trajectories are the movements of the targets in the *image* space only and not the real movements in *3D* space, which are distorted due to the Doppler shift.

In the following, we briefly introduce the MiSAR sensor and its specifications as well as the test area. Then the method is described in detail. Beginning with the SPECAN-processed OAwrB images, we will focus on the extraction of potential moving objects in each OAwrB and subsequently use these observations to integrate the findings in a general tracking framework to obtain the trajectories of the moving objects over time. We describe the results obtained on the MiSAR data set and conclude with potential future research and applications.

II. Method

A. Test site and sensor

The study area is located south of the city of Ulm in southern Germany. In Fig. 1 the focused geocoded single-channel SAR image is overlaid on a topographical map. The strip is ~2450 m long and ~850 m wide. Two highways, one with along-track and one with cross-track orientation, are present: they serve as the main areas for testing the tracking method.

Manuscript received July 18, 2011; revised January 10, 2012. This work was supported in part by armasuisse W+T.

The authors are with the Remote Sensing Laboratories, Department of Geography, University of Zurich, CH-8057 Zurich, Switzerland (phone: +41-44-6356524; fax: +41-44-6356846; e-mail: daniel.henke@geo.uzh.ch).

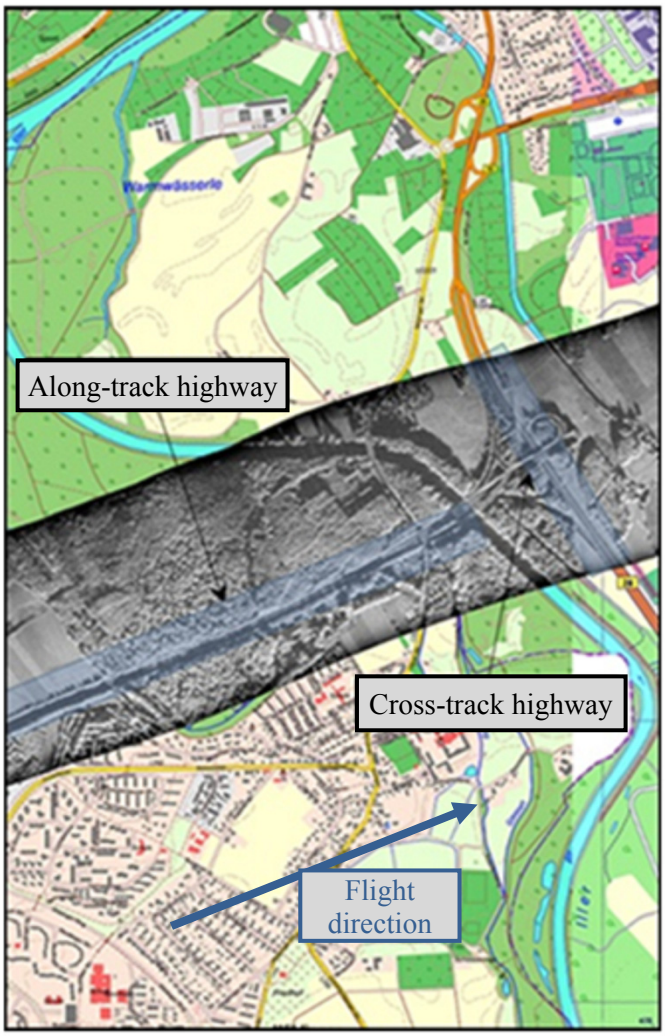

Fig. 1. Test site in South Germany: Topographic map overlaid with the focused SAR image with the two main highways investigated for moving object tracking.

The sensor system used for the experiments is the frequency-modulated continuous-wave (FMCW) Miniature Synthetic Aperture radar (MiSAR) system, developed by EADS, Germany [14], [15]. It is a small lightweight system that operates at 35 GHz in Ka-band and can be mounted on Unmanned Aerial Vehicles (UAVs) or small manned aircrafts. The sensor's azimuth beam width for the experiment is ~14° and the pulse repetition frequency (PRF) 2000 Hz, with resolution ~0.5 m in range and azimuth. The MiSAR's slant range is approximately three times the cruise altitude. In the experiment discussed, the slant range was ~1500 m.

B. Overview of the processing chain

The proposed method for tracking moving targets in SAR data with a wide beam sensor can be subdivided into three major parts. The first task is to process and geocode the SAR data to OAwrB images. The tracking algorithm works independently of the focusing algorithm. We use the SPECtral ANalysis (SPECAN) algorithm ([21], [22]) to focus the OAwrB images, as it is an ideal burst processing method for low bandwidth images. Having obtained a sequence of images where static targets stay at the same position while the moving targets are displaced over time, we collect image statistics and use image processing methods to extract potential moving objects in each image. The candidate objects are based only on single images, with the temporal behavior ignored at this stage. In the third processing step, we use a multi-target unscented Kalman filter approach incorporating a dynamic model to associate the extracted time-independent observation of step two to generate maximum probability moving target trajectories. An overview of the processing chain can be found in Fig. 2.

C. Processing and geocoding the raw data

In preparation for the tracking algorithm, the OAwrB images are first processed. They have an azimuth extent of 250 m - 300 m, determined by the azimuth beam width and slant range. An implicit tradeoff is made between a low bandwidth with a higher energy concentration of moving vs. static targets vs. a high bandwidth with a better image resolution. We chose short bursts of only 0.25 s, corresponding to ~8 m synthetic aperture length, i.e. around 2% of the full synthetic aperture, resulting in a good energy conservation of moving targets while also offering a reasonable spatial resolution (~1 m). A compromise has to be made between (a) a high overlap implying a high temporal resolution and thus an improved tracking reliability, and (b) computation time. We chose an overlap between the OAwrB images of ~90% (step width: 0.0195 s).

Preprocessing steps such as Kalman filter based GPS/INS integration, track linearization including first order motion compensation, range cell migration correction (performed in the range-Doppler domain) and side-lobe suppression are performed before the SPECAN algorithm can be applied. SPECAN, a burst processing method ideal for OAwrB images, is a very computationally efficient method. It directly delivers a focused image for nearly the entire illuminated footprint, also in the azimuth dimension, using a short azimuth segment (or burst), where the azimuth extent of the processed image is much larger than the burst length. SPECAN is significantly less computationally demanding than other stripmap processing methods such as range-Doppler, Ω-k or chirp scaling.

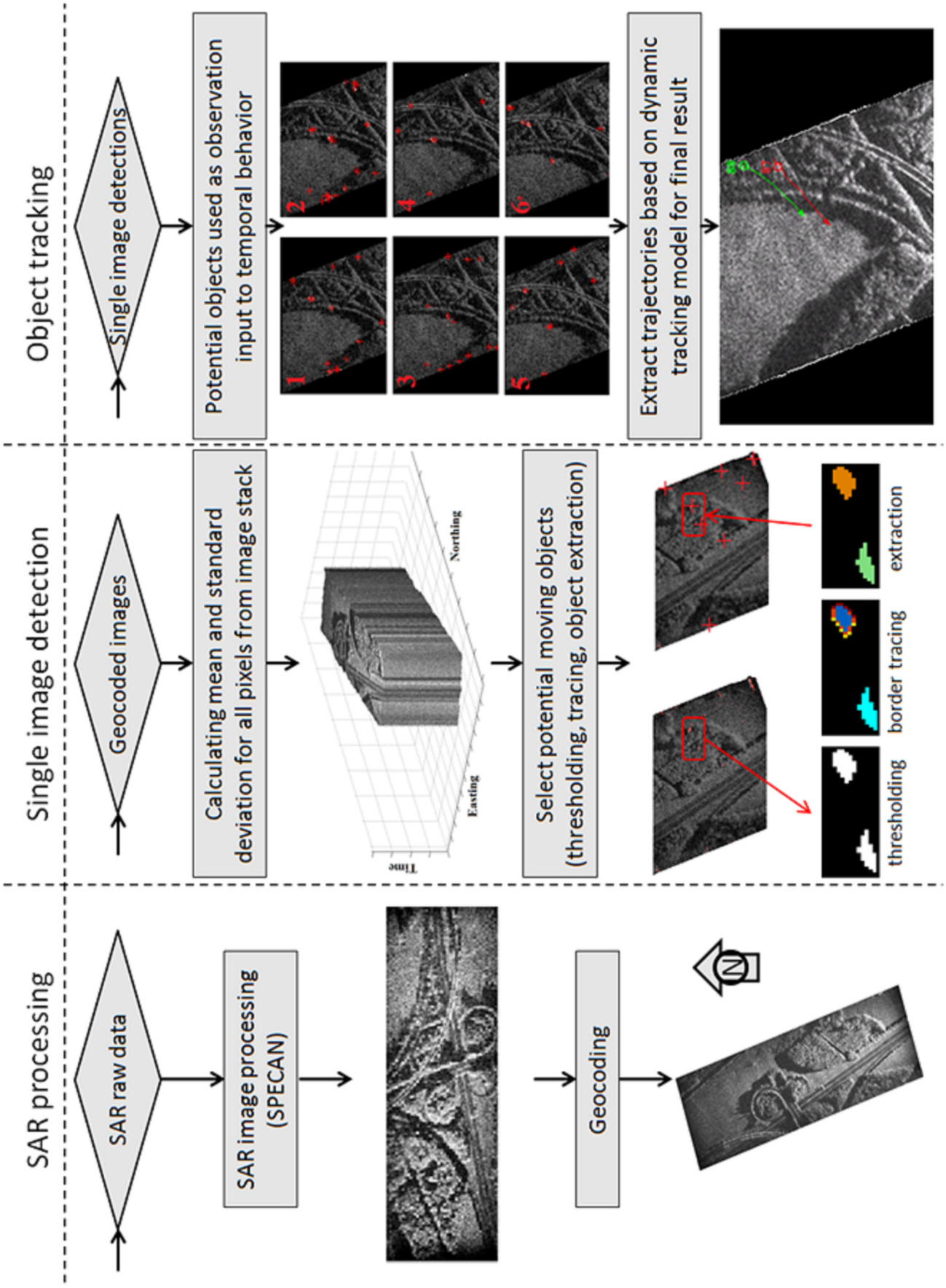

Fig. 2. Flow-chart of the processing chain

The use of SPECAN in the past [21], [22] has often been restricted to narrow antenna beam-widths and small squint angles (i.e. satellite sensors). We implemented an algorithm described in [23] for wide-beam airborne sensors, briefly summarized here. The most important assumption made in SPECAN is that the Doppler rate should be constant for any target during the whole of its integration time and that this rate is constant for all targets at the same slant range. While the Doppler centroid is deduced from the navigational data, the Doppler rate is taken as its instantaneous value for a target at a given slant range and a given squint angle associated with the Doppler centroid relative to the linearized track. With the previously mentioned constant Doppler rate assumption, all targets at the same slant range have similar Doppler histories. Plotting the Doppler centroid versus azimuth time, these histories are approximated by straight lines with the slope of the Doppler rate (ramps). The principle of SPECAN is based on the observation that the position of any target (or equivalently its azimuth time) is uniquely determined by its frequency value at some reference time. This equivalence makes it possible to reduce the required processing to only two steps, namely de-ramping and spectral analysis. The de-ramping transforms the Doppler history into constant frequency lines, and the spectral analysis maps these frequency components to the azimuth time. The spectral analysis is performed through a Scaled Fourier Transform implemented via fast-convolution using the Chirp-Z Transform as described in [24]. Compared to the basic variant of SPECAN using a simple Fourier Transform, this has the advantage of producing images with an azimuth pixel spacing independent of range, therefore avoiding the need to interpolate the data at the final stage. In addition, the azimuth pixel spacing can be adjusted using a scale factor.

Finally, tracking the target requires that the stack of images share a common geometry. The OAwrB images are geocoded once they have been focused with the SPECAN algorithm to provide the position and velocity of the moving targets in a geodetic coordinate system. For the geocoding, first a set of points around the perimeter of the focused image is projected into a map geometry using a forward geolocation algorithm. Then a region of interest containing the coordinates of these points plus a margin is defined and a regular grid in local map coordinates is created in this region of interest. Finally, the image samples are extracted from the input data using a standard backward geocoding algorithm. Both forward and backward geocoding processes are based on a standard range-Doppler approach [25] using a Digital Elevation Model (DEM) and all necessary geodetic and cartographic transformations and parameters. A detailed description of this algorithm can be found in [23].

The geocoded images have a pixel-spacing of 0.5 m and were evaluated to analyze the internal accuracy of the geocoding procedure. Since no reflectors were deployed in the campaign, three bright static targets on a dark concrete area were used to estimate the geolocation accuracy, relevant for the later detection and tracking algorithm. The standard deviation of these static targets varies between 0.51 m and 1.37 m in northing and between 0.94 m and 1.86 m in easting over the whole sequence of images where the static targets were in the antenna beam. The image to image shift of the geolocation is on average 0.06m in northing and 0.18m in easting. The accuracy of the geocoded images is most reliable in the center of the images and degrades to towards the edges. Causes of error are inaccurate navigation data, motion compensation of small flight track segments and also SPECAN algorithm uncertainties at the image edges (mainly azimuth dimension). Nevertheless, the variations in the relative image-to-image positions are sufficiently accurate for our detection and tracking purposes.

D. Extraction of moving target candidates

After the raw data focusing to geocoded OAwrB images, one obtains an image stack *S(m,n,t)* over time for which the following statement holds:

Let $I_t(m,n)$ be the OAwrB geocoded amplitude image at time t.

$$S(m,n,t) = \begin{cases} I_t(m,n) & \begin{array}{l} if\ the\ pixel\ at \\ position\ (m,n)\ is\ a \\ valid\ pixel\ in\ image\ I_t \end{array} \\ undefined & otherwise \end{cases} \quad (1)$$

From Eq. (1) one can derive the mean and standard deviation of each pixel's intensity over time:

$\forall m,n$:

$$\bar{S}(m,n) = \frac{\sum_{\forall t:S(m,n,t)\neq undef} S(m,n,t)}{\sum_{\forall t:S(m,n,t)\neq undef} 1} \quad (2.1)$$

$$\sigma(m,n) = \sqrt{\frac{\sum_{\forall t:S(m,n,t)\neq undef} (S(m,n,t) - \bar{S}(m,n))^2}{\sum_{\forall t:S(m,n,t)\neq undef} 1}} \quad (2.2)$$

As we approximate the mean and standard deviation based on pixel samples, it is clear that with increasing numbers of samples the reliability of the estimated statistics and thus the detection probability of potential moving objects improves. This increase in the number of pixel samples is dependent on the pixel's beam dwell time and is consequently best achieved by using a wide beam sensor where our proposed method works independently of the acquisition mode. With minor adaptations the method could also be applied to sensors with a narrower azimuth beam width using spotlight mode to achieve longer dwell times.

From the statistics calculated in Eq. (2), we can derive the outlier pixels with high positive variance that indicate the presence of non-static pixels at specific OAwrB instances:

$B(m,n,t)$ is defined as a Boolean matrix with value 1 for potential moving pixels and 0 otherwise.

$$B(m,n,t) = \begin{cases} 1 & if\ S(m,n,t) > \bar{S}(m,n) + \alpha\sigma(m,n) \\ 0 & otherwise \end{cases} \quad (3)$$

The value of α specifies the threshold that determines which pixels are treated as candidate moving objects. The parameter α is a sensor-specific property and was chosen on an experimental basis. In theory, the parameter could be derived from an extensive calibration data take, overflying the same restricted control area twice – once with and once without moving objects – to estimate the optimal value for α. However, experiments have shown that the choice of α is not critical providing that it stays within a certain range. We set $\alpha=4.5$ in our MiSAR experiment, providing an appropriate

tradeoff between false positive detections and missing candidates.

Until this point, we have been dealing with a pixel-based matrix, but to obtain a set of potential moving object candidates at each time step, we next make use of segmentation algorithms to group single pixels into connected object areas. First of all, morphological open and close operations are conducted to reduce noise in the Boolean matrix B. A morphological reconstruction based on the new matrix B and S is then performed to connect neighboring objects that have a high positive variance on a connecting path. An efficient morphologic reconstruction is described in [26]. For each image at time t, B_t acts as a seed point mask and S_t as a marker image to obtain S_t^{new} which is used to calculate B_t^{new} equivalent to Eq. (3), using a slightly lower threshold α_2 (in our MiSAR experiment: α_2=3.5). Fig. 3 illustrates the output of the algorithm for a particular time.

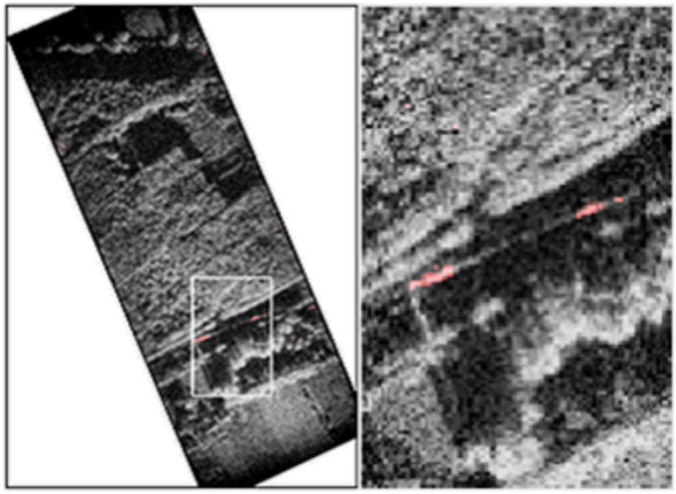

Fig. 3. Pixel areas marked as potential moving objects after morphological reconstruction.

Finally, one has to extract connected objects from the Boolean pixel mask. We use an extraction algorithm based on border tracing as described in [27]:

Let *(p,r)* be the first spatial edge where a 0/1 switch occurs: (4.1)

$$B_t(p,n) = 0 \rightarrow B_t(r,n) = 1$$

Let $\xi(p)$ be the 4-neigborhood of p in circular order:

$\xi(p) = \{\rho_0, \rho_1, \rho_2, \rho_3 = r\}$ with the 4-neigborhood being defined as follows: (4.2)

$$\begin{bmatrix} * & \rho_0 & * \\ \rho_3 & p & \rho_1 \\ * & \rho_2 & * \end{bmatrix}$$

Find the first $r^* := \rho_k$ in $\xi(p)$ where $\rho_k = 1$ holds: $\min_{0 \le k \le 3} \rho_k = 1$ (4.3)

and add r^* to the list of border points.

If r^* is equal to the initial point of Eq. (4.1) the complete object border was traced and the next 0/1 switch in the image needs to be found to extract the next object starting from Eq. (4.1). Otherwise, set $r = p$ and $p = r^*$, and repeat steps (4.2) and (4.3) until r^* equals the initial point of (4.1):

$$r^* == initial\ p\ ? \begin{cases} yes & \rightarrow algorithm\ finished,\ object\ border\ traced \\ no & \rightarrow r := p, p := r^*\ and\ proceed\ with\ Eq.(4.2) \end{cases} \quad (4.4)$$

Thus, one obtains a set of objects for each binary image B_t indicating potential moving objects. This set of moving object candidates includes a considerably higher number of (false) detections than the final detection set after the tracking model is applied. The reasons are (a) the relatively low values for the threshold α and the processed bandwidth of the OAwrB which enable detection of objects with low Radar Cross Section (RCS)[1] at the cost of a higher number of false detections in single OAwrB images and (b) speckle noise effects. Fortunately, the dynamic modeling of the temporal tracking successfully suppresses most of these misdetections given that non-moving detections (e.g. speckle noise, static above-threshold detections) appear randomly or completely static in the image space thus lacking any dynamic behavior over time and therefore getting identified as clutter by the tracking model. For each object, characteristics like the center of mass and the area are calculated. The area can be used to eliminate small objects most likely caused by noisy artifacts. Additional object characteristics might be useful for the tracking algorithm but were not investigated in this work. The center of mass illustrated in Fig. 4 is used as the "raw" observation for the Kalman tracking approach discussed in the next section when considering temporal behavior.

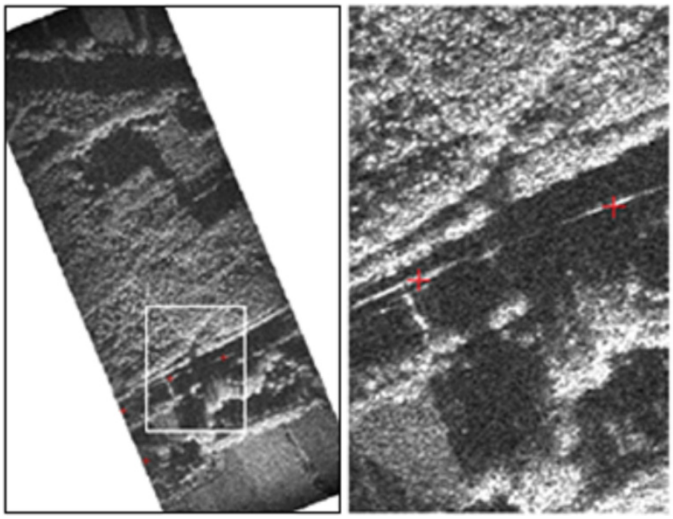

Fig. 4. Output of the center of mass points serving as observations for the multitarget Kalman filter approach. Time step is the same as in Fig. 3.

E. Tracking of the moving objects

A broad overview of multi-target tracking algorithms is provided in [28]. The advanced multi-target tracking algorithm we investigate in this paper is based on the theory of unscented Kalman filtering (e.g. [29], [30]) and sequential

[1] To calculate the ranges for objects that are detectable is impracticable as it depends on factors like its RCS, orientation, moving direction, speed (i.e. energy concentration), background clutter, location within the antenna beam etc.

Monte Carlo methods (e.g. [31]) in general, and on a combination of both for multi-target tracking specifically on a work by S. Särkkä et al. [32]. The tracking approach developed by Särkkä et al. outperforms several multi-target tracking methods in accuracy and computational efficiency. For a detailed comparison with classical multi-target tracking approaches with a fixed number of targets, see [33]. The basic framework for SAR moving target tracking using multi-target unscented Kalman filters was previously introduced and demonstrated for a simplified simulated data set in [20]. For the real data experiments, two major changes have been made compared to the previous work: first, while in [20] we developed a tracking method for simulated multi-static data, we deal here with a monostatic real data experiment, implying some presumptions concerning the movement of the objects: we assume the moving objects to be at ground level and have only moderate non-linear motion and acceleration events. Thus, we can estimate the moving target's position based only on monostatic acquisitions. Second, the extraction of potential moving targets tuned for the MiSAR sensor (see III.B) is now integrated into the tracking framework: several adaptations to the Kalman filter model were necessary.

In the following, we summarize the computational chain, explaining the parameters used within the tracking algorithm.

i) Filtering models and the Unscented Kalman Filter (UKF)

Kalman filters are time discrete filters modeled with Markov chain properties and additional Gaussian noise to estimate the hidden state of a dynamic system from noisy observations. An iterative estimation-maximization approach is used to find the optimal hidden state estimate at each time step. Thereby, the unscented Kalman filter is an extension of the standard Kalman filter allowing non-linear state transitions and transformation functions. This is realized by the so-called unscented transformation ([34],[35]).

For the unscented transformation, we consider a random variable ψ (of dimension L) with mean $\bar{\psi}$ and covariance C_ψ propagated through a nonlinear function $y = g(\psi)$. To calculate the transformed random variable y, we first select $2L+1$ sigma points ψ_i with corresponding weights w_i as defined in the following equations (5.1) and (5.2):

First, form the sigma point matrix $\Psi = [\psi_o^T \dots \psi_{2L}^T]^T$

$$\begin{aligned} \psi_0 &= \bar{\psi} \\ \psi_i &= \bar{\psi} + \left(\sqrt{(L+\lambda)C_\psi}\right)_i \qquad i = 1, \dots, L \\ \psi_i &= \bar{\psi} - \left(\sqrt{(L+\lambda)C_\psi}\right)_{i-L} \quad i = L+1, \dots, 2L \end{aligned} \tag{5.1}$$

Form the mean $W^{(m)} = \left[w_0^{(m)T} \dots w_{2l}^{(m)T}\right]^T$ and the covariance $W^{(c)} = \left[w_0^{(c)T} \dots w_{2l}^{(c)T}\right]^T$ weights:

$$\begin{aligned} w_0^{(m)} &= \frac{\lambda}{L+\lambda} \\ w_0^{(c)} &= \frac{\lambda}{L+\lambda} + (1 - \alpha^2 + \beta) \\ w_i^{(m)} &= w_i^{(c)} = \frac{1}{2(L+\lambda)} \qquad i = 1, \dots, 2L \end{aligned} \tag{5.2}$$

$\lambda = \alpha^2(L+\kappa) - L$ is a scaling parameter, α determines the spread of the sigma points around $\bar{\psi}$ (usually a small positive value, e.g. 0.001), κ is a secondary scaling parameter (set to 0) and β is used to incorporate prior knowledge of the distribution of ψ (for a Gaussian: $\beta = 2$). The lower index i indicates the ith row of a matrix. These sigma points are then interpreted using the non-linear function g: $\mathcal{Y}_i = g(\psi_i)$. The transformed $\mathcal{Y}_i$'s are used to approximate the *a posteriori* distribution of the random variable y:

Weighted sample mean

$$\bar{y} \approx \sum_{i=0}^{2L} w_i^{(m)} \mathcal{Y}_i \tag{5.3}$$

Weighted sample covariance

$$C_y \approx \sum_{i=0}^{2L} w_i^{(c)} (\mathcal{Y}_i - \bar{y})(\mathcal{Y}_i - \bar{y})^T \tag{5.4}$$

This approximation preserves at relatively low computational cost accuracy to the third order for Gaussian inputs for all nonlinearities and thus outperforms other non-linear Kalman filter approaches as e.g. the extended Kalman filter. By using the unscented transformation we can use arbitrary non-linear state transition and transformation functions for the Kalman filter to propagate the state and covariance matrix forward in time. The state transition function

$$x_k^- = f(x_{k-1}, q_k) \text{ with } q_k \sim N(0, Q_k) \tag{6.1}$$

projects the estimated hidden state forward in time. q_k models the process noise; x_{k-1} and x_k^- are the states at the previous time step *k-1 after* the observation update and the current time step *k before* the observation update, respectively. This part of the iterative procedure is called the *prediction* step. In the *update* step, a new observation is made at time step k and the current state x_k^- is updated according to the transformation function

$$z_k = h(x_k^-, v_k) \text{ with } v_k \sim N(O, R_k) \tag{6.2}$$

which maps the state x_k^- *before* the observation into the observation space Z with v_k modeling the uncertainty of the observations. This function is used to calculate the Kalman gain K_k and update the state x_k to obtain the most probable state estimate considering the observation at time step k.

In our experiments, the state x is defined as:

$$x = \begin{pmatrix} pos_{east} \\ pos_{north} \\ V_{abs} \\ \varphi \end{pmatrix} \tag{6.3}$$

with pos_{east} and pos_{north} being the map coordinates of the object [m], V_{abs} the absolute velocity [m/s] and φ the direction of movement [°]. The transformation function mapping from the state into the observation space is in our case linear:

$$h(x) = Hx \tag{6.4}$$

with x being the state and $H = \begin{pmatrix} 1 & 0 & 0 & 0 \\ 0 & 1 & 0 & 0 \end{pmatrix}$ the transformation matrix. The extracted centers of mass in the observation space correspond to the coordinates pos_{east} and pos_{north} of the state.

The non-linear state transition function feeding forward the state x in time t is defined in our experiment as follows:

$$f(x) = \begin{pmatrix} pos_{east} + t * cos(\varphi) * V_{abs} \\ pos_{north} + t * sin(\varphi) * V_{abs} \\ V_{abs} \\ \varphi \end{pmatrix} \quad (6.5)$$

Eq. (6.3)-(6.5) define the fundamental parameters of the Kalman filters. For the complete definition, the initial values for the state x_o and its associated covariance matrix C_0 as well as the observation noise R and process noise Q must also be set appropriately. The positions pos_{east} and pos_{north} are initialized to the coordinates of the center of the geocoded SAR image. For the absolute velocity V_{abs}, a value of 30 m/s (108 km/h) is chosen as a best initial estimate of the velocity of vehicles on the highway. The initial direction φ can have an arbitrary value, as no prior knowledge about the main driving direction of the vehicles is available. We account for the arbitrary direction value by setting the initial covariance matrix C_0 with a quasi uniformly distributed direction, equivalent to a very high value for the diagonal value of C_0 associated with the direction. Also for the diagonal values of C_0 affecting the positions we choose a quasi uniform distribution over the complete valid area of the SAR image given that we have only limited knowledge of the "birth" position of moving objects. The diagonal value of C_0 affecting the absolute velocity is set to 100, equivalent to a standard deviation of 10 m/s implying an initial guess that ~68% of the vehicles move with a speed between 20 – 40 m/s (72 – 144 km/h) and ~95% between 10 – 50 m/s (36 – 180 km/h). Non-diagonal values of C_0 are set to 0. For the observation noise R, the diagonal values are set to 25, implying a standard deviation of 5m in northing and easting of the observations, respectively, reflecting a realistic uncertainty after visual inspection of the results of the method in III.B. Finally, the process noise matrix Q has to be defined. The diagonal values in Q associated with the position values of the state are set to low values of 0.01m. The state transition function of the model implies uniform and linear dynamic behavior of the moving objects, but we want to be able to track non-uniform, non-linear targets, so we allow as a noise component a standard deviation of 0.5° for the value associated with the movement direction (this favors linear movement as highway vehicles are assumed to be moving mainly straight but allows a degree of non-linearity) and a standard deviation of 1.5 m/s for the value associated with the absolute velocity V_{abs}, to realistically model vehicular acceleration and slowdown events. We use a model that assumes uniform, linear movement only to keep the number of parameters for the state low and thus more robust. However, by allowing some noise component for the moving direction and a relatively high noise level in the velocity, non-linearity as well as acceleration events are handled well within realistic boundaries.

ii) Tracking multiple moving objects

The Kalman filter described above handles an accurate tracking of one vehicle. An open problem remains the tracking of multiple objects in the presence of clutter, equivalent to associating each observation to the correct tracking history or identifying it as clutter. This is done based on Rao-Blackwellized particle filtering [32], relying on an extended Markov Chain Monte Carlo (MCMC) sampling technique to best approximate the posterior distribution for the data association to the set of Kalman filters. In the following, we briefly describe the main steps of the processing chain to understand the parameters used for our test data set. The problem can be subdivided in to two tasks. The first task is to find the correct association of a new observation under the assumption of a known number of targets. This is, generating the optimal importance distribution for all particles according to the Rao-Blackwell theorem:

$$p(d_k \mid z_{1:k}, d_{1:k-1}^{(i)}) \quad \forall particles\ i \quad (7.1)$$

which is the probability of the association d_k given the association history $d_{1:k-1}^{(i)}$ and all observations $z_{1:k}$ up to and including time step k. Using Bayes rule, we can derive:

$$\begin{aligned} &p(d_k \mid z_{1:k}, d_{1:k-1}^{(i)}) \propto \dots \\ &\dots\ p(z_k \mid d_k, z_{1:k-1}, d_{1:k-1}^{(i)}) \times p(d_k \mid d_{k-m:k-1}^{(i)}) \end{aligned} \quad (7.2)$$

where $p(z_k \mid d_k, z_{1:k-1}, d_{1:k-1}^{(i)})$ is given by the clutter density function $p_{clutter} \coloneqq p(z_k \mid clutter)$ for the case of d_k being clutter and by the Kalman filter measurement likelihood evaluation of the Kalman filter associated to d_k otherwise. According to Eq. (7.2), we can use sampling techniques to approximate the posterior distribution for the data association.

In the second task, we deal with an unknown number of targets, which are "born", exist for a while and then "die" again. It is realized by allowing a very high number of targets in the model (in theory infinite; in practice the maximal conceivable number). The probability of a target's birth is derived from the clutter probability and the detection probability p_{detect}, and its life time t_d is modeled by a gamma distribution Γ indicating the time a target is active (i.e. the typical time of a target existence).

For the clutter density function $p_{clutter}$, a uniform distribution in the measurement space is chosen and the detection probability p_{detect} is set to 0.6. For the lifetime t_d we use a gamma distribution with a peak at a duration of 1.5s and a smooth gradient allowing a quite wide range of target lifetimes, accounting for the fact that targets moving in the cross-track direction remain in the images for longer periods than targets that move along-track.

The setting of the parameters is done based on prior knowledge and observations, relying also on human expertise and testing to tune the method for optimal performance. The choice of parameters is optimized for the specific MiSAR experiment and has to be adapted for other sensors. Note that the parameters are set very generically to allow a very general tracking framework. Additional prior knowledge can improve performance further at the cost of generality. This could e.g. be done by a reduction of potential "birth" locations by excluding large forested or other roadless areas.

III. Results of the MiSAR experiment

We applied the above method to the MiSAR data set described in section II. Two factors were unfavorable for our experiments. First, no ground truth was acquired during the campaign, implying that only rough estimates of the real speed of a vehicle can be used for validation. Second, the grazing angle of the sensor is low (~18°). The forested areas on both sides of the highway therefore cause shadow and layover effects, significantly impairing the detection of moving targets

in these regions. However, the MiSAR sensor with its wide antenna beam and the test area are well suited to the task of tracking moving objects in a sequence of OAwrB images.

One hundred and fourteen objects were detected; the tracks are indicated in Fig. 5.

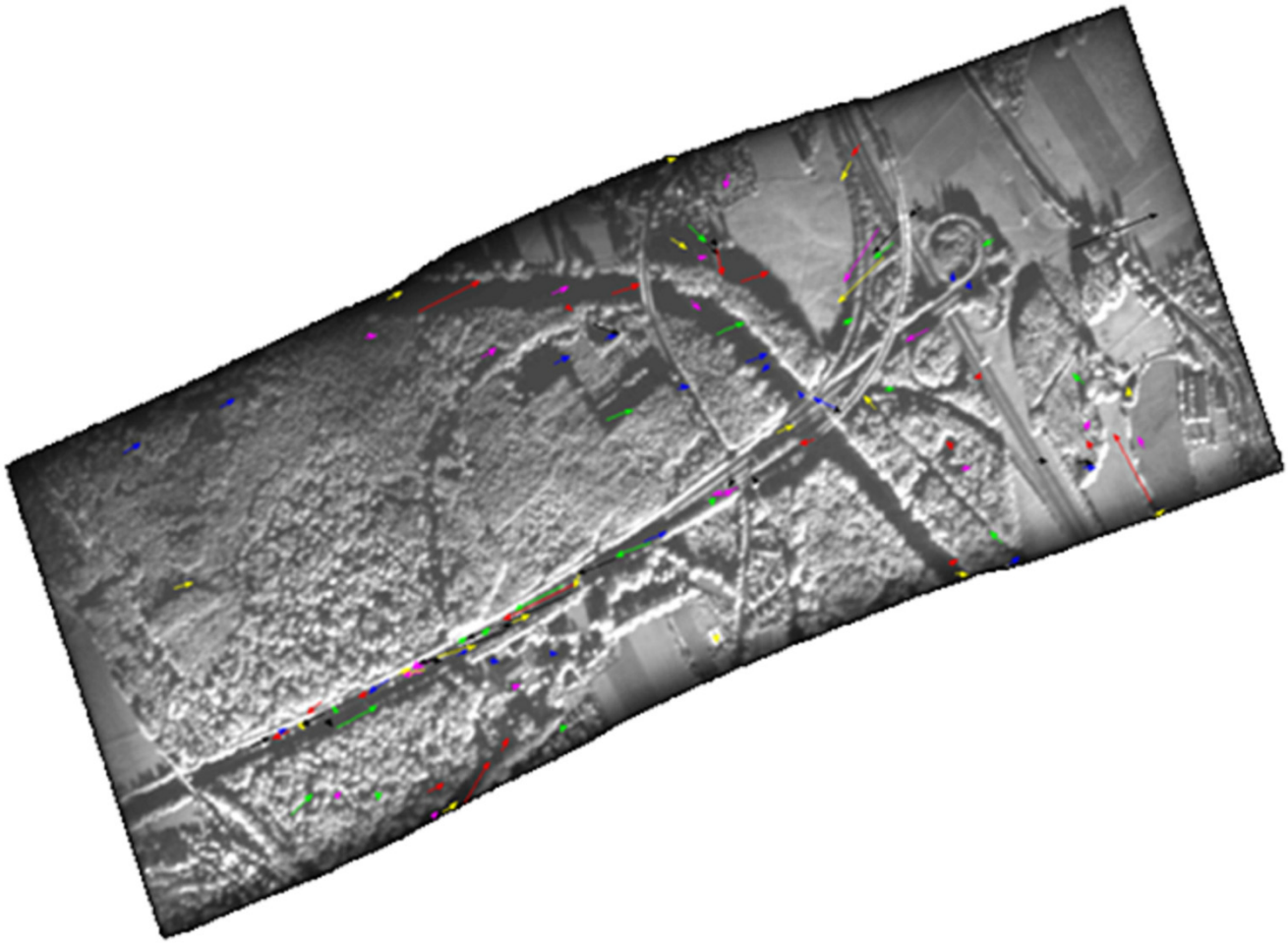

Fig. 5. The output of the 114 detected objects and the associated movements for the complete scene. The arrows indicate the beginning and end of the movements; the usage of different colors helps keep targets separable. An agglomeration of objects along the highways is clear.

Additional post-processing not discussed in this paper might be able to exclude some artifacts caused mainly by noisy observation at the edges of the images (lower signal-to-noise ratio) and processing artifacts in the OAwrB images. In the following we use the estimated velocities of the vehicles in the *image* space as rough approximations of the true *3D* velocities to evaluate our method without applying any *image to 3D velocity* corrections. This allows meaningful comparisons between image and 3D velocities only for cross-track moving objects. We comment on possible ways to transform the image space velocities distorted by the Doppler effect to 3D velocities later in the paper. The Doppler corrections are not part of this paper, as (a) we do not have ground truth velocities to calculate reliable error bars even after performing a Doppler shift correction, (b) the accuracy of the navigation data is insufficient (no differential GPS (dGPS) data available) and (c) the MiSAR sensor is a high-frequency sensor, thus inducing significant additional uncertainty to *image to 3D space* transformations. The sensor has a wavelength of 8.69 mm and a PRF of 2000 Hz, the Doppler ambiguity equates to a radial velocity difference of only 8.69 m/s. With a slant range of roughly 1500 m, a platform speed of ~35 m/s and an inaccuracy of 1 m/s in radial velocity, the Doppler shift is given by [7]:

$$\Delta azimuth = -\frac{V_{radial}}{V_{platform}} * \left|\overrightarrow{Range}\right| \approx -43m \qquad (8.1)$$

The above relation implies that especially for targets moving mainly in the along-track direction, the velocity estimates are distorted, as even a small Doppler shift in the azimuth direction has a large influence on the velocity as the direction of the shift is parallel to the object's direction of movement. For cross-track moving objects, the shift in the absolute position is much larger as the radial velocity of cross-track moving objects is larger. However, its distortion of the velocity between image and 3D space is considerably smaller, as the direction of movement and the Doppler shift are perpendicular and the relative change of the radial velocity (and Doppler shift, respectively) between the first and last detection of the object (in the first and last OAwrB/burst) is smaller than for objects moving opposite to the sensor's movement in along-track direction.

In the following, we discuss three exemplary cases (shown in Fig. 6(a)) to demonstrate the algorithm's output in the image space.

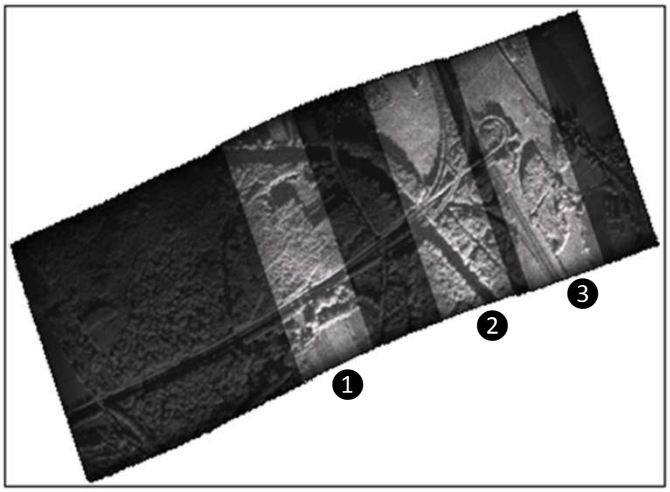

(a) Locations of the three exemplary cases.

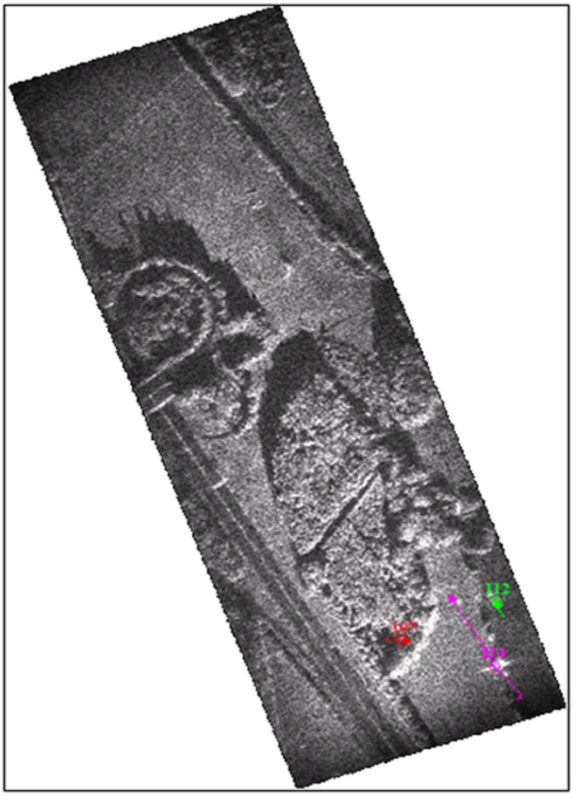

(b) Scene 3 of Fig. 6(a): Three moving targets; the longest movement of object 114 is mainly in the cross-track direction.

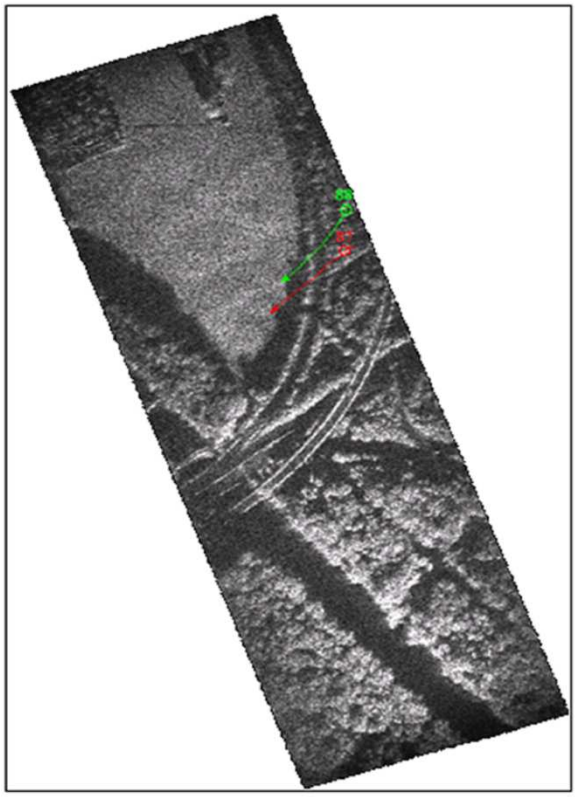

(c) Scene 2 of Fig. 6(a): Two moving targets with a cross- and along-track direction of the movement.

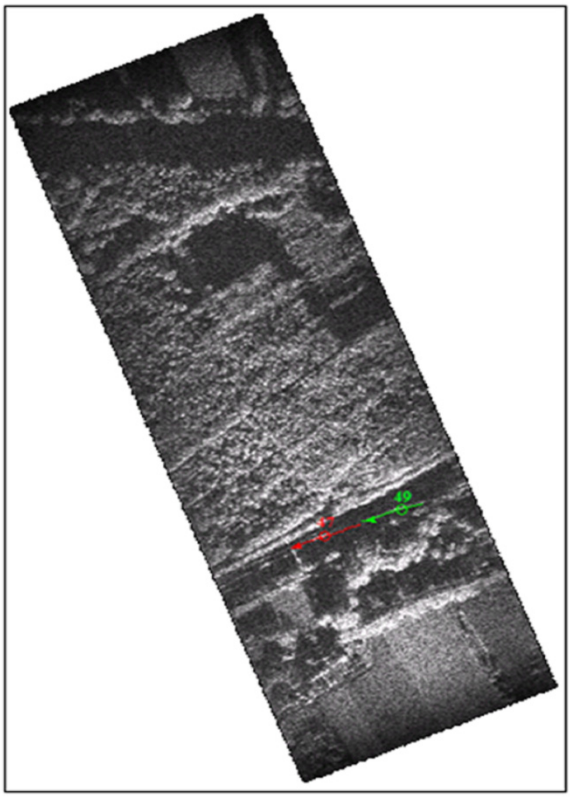

(d) Scene 1 of Fig.6(a) with two targets moving in the along-track direction on the highway.

Fig. 6. Three selected cases for the output of the tracking algorithm. The circles indicate the positions at the current time step and the arrows the movement for the time the objects are detected in the beam of the radar sensor.

Fig. 6(b) illustrates the trajectories of three moving vehicles (with identification number). Target 114 is moving in the cross-track direction (implying large positional and small velocity distortions introduced between image and 3D space); the estimated image velocity of 28.87 m/s (~103.9 km/h) is a realistic 3D velocity. This object has the longest dwell time (4.70 s). The real world position of object 114 is most probably the highway about 143m west of the detected position in the image space. Fig. 6(c) shows two vehicles (ID: 87 and 88) moving in a diagonal direction to the cross-/along-track. They are tracked for 2.40 s and 2.93 s, respectively; their real positions are probably on the on-ramp southeast of their image positions. As they have a non-negligible along-track direction component in their movement, the estimated target velocities are distorted with values around 40 – 45 m/s (144 – 162 km/h). Their image velocities are surely overestimating the 3D velocities for this road section. We obtain even higher values of over 70 m/s (252 km/h) for the vehicles number 47 and 49 in Fig. 6(d) moving predominantly in the along-track direction. These values are distorted by a Doppler shift (which is small in absolute values but with larger relative changes between first and last detection and parallel to the moving direction thus directly influencing its velocity estimate). The image positions of the vehicles are only slightly shifted, as the radial velocity component for targets moving along-track is considerably smaller; this is why they are mapped on the highway, probably shifted only slightly to the south.

The results from the test data set seem promising and accurate in the image space; unfortunately, evaluation of the results based on 3D space velocities is difficult due to the sensitivity of the Doppler shift to the radial velocity because of the high frequency sensor and imprecise navigation data and due to the lack of ground velocity measurements. To give the reader an impression of the accuracy, we summarize the algorithm's output in a visual evaluation (Table 1, note: velocities are only given for cross-track targets as they are better approximations of their 3D velocities; misdetections are almost exclusively caused by processing artifacts, e. g. glint points, and noise effects at the edges of the OAwrB).

We additionally tried to visually identify objects not detected by the algorithm, finding 25. The derived statistics are summarized in Tables 2 and 3.

Although this is not an absolute validation of the method, these results with single channel SAR data demonstrate good performance of the algorithm as far as possible in the absence of ground truth data (classification probability of ~72% with a false alarm rate of only ~33%). Furthermore, in Fig 7. characteristics of the detected moving objects are illustrated. The distribution of the speeds of cross-track moving objects (varying between 10 m/s and 35 m/s, Fig. 7(a)) and the distribution of the direction of movement which is dominated by the coincident highway direction (Fig. 7(c)) give additional indications of successful velocity estimations in the image space.

TABLE 1
VISUAL EVALUATION OF THE TRACKING ALGORITHM

TID	TT	MD	MV	R?	TID	TT	MD	MV	R?
1	0.84	21.88	n/a	no	58	1.11	-4.82	n/a	yes
2	0.86	10.01	n/a	no	59	0.45	99.87	14.35	yes
3	0.9	-2.56	n/a	no	60	1.25	-2.56	n/a	no
4	0.49	33.48	n/a	no	61	0.62	81.49	14.89	yes
5	1.38	7.73	n/a	?	62	0.55	-4.12	n/a	?
6	0.43	2.3	n/a	yes	63	0.9	0.63	n/a	no
7	0.47	48.31	n/a	no	64	0.43	-2.76	n/a	no
8	0.45	1.25	n/a	?	65	0.49	38.91	n/a	yes
9	0.45	96.89	26.44	?	66	0.47	-4.62	n/a	yes
10	0.47	34.98	n/a	no	67	1.42	-0.74	n/a	no
11	0.66	4.15	n/a	yes	68	1.09	-2.02	n/a	no
12	0.7	13.14	n/a	yes	69	0.92	-1.25	n/a	no
13	0.59	100.51	21.09	?	70	0.66	3.81	n/a	yes
14	0.7	8.31	n/a	no	71	0.49	87.88	13.65	no
15	0.92	-6.94	n/a	yes	72	1.68	-4.26	n/a	no
16	0.45	-12.91	n/a	yes	73	1.17	119.75	n/a	yes
17	0.53	108.21	n/a	?	74	0.51	25.39	n/a	yes
18	0.62	-2.07	n/a	yes	75	0.66	116.75	n/a	?
19	1.99	5.63	n/a	yes	76	0.76	116.62	n/a	yes
20	0.82	13.36	n/a	yes	77	1.07	117.9	n/a	yes
21	0.84	1.87	n/a	yes	78	0.53	8.64	n/a	no
22	0.47	2.63	n/a	yes	79	0.7	4.75	n/a	yes
23	1.7	-1.3	n/a	yes	80	3.06	138.12	n/a	yes
24	0.9	5.39	n/a	no	81	1.03	130	n/a	yes
25	0.47	46.86	n/a	yes	82	0.8	55.07	n/a	yes
26	0.6	158.05	n/a	?	83	0.47	118.16	n/a	yes
27	0.9	13.4	n/a	no	84	1.29	84.27	36.22	yes
28	0.43	27.85	n/a	yes	85	0.43	-11.99	n/a	yes
29	0.92	-16.6	n/a	yes	86	1.19	102.53	7.92	?
30	2.2	36.67	n/a	no	87	2.4	20.96	n/a	yes
31	0.49	6.77	n/a	yes	88	2.93	33.16	n/a	yes
32	0.62	13.52	n/a	?	89	0.84	18.62	n/a	yes
33	2.48	-4.95	n/a	yes	90	0.57	40.39	n/a	yes
34	0.64	-8.91	n/a	no	91	1.31	13.34	n/a	yes
35	2.16	1.1	n/a	yes	92	0.53	59.44	n/a	?
36	0.6	40.48	n/a	no	93	0.88	42.36	n/a	yes
37	0.62	22.27	n/a	yes	94	0.7	3.39	n/a	yes
38	0.49	151.34	n/a	?	95	1.48	22.91	n/a	yes
39	0.62	5.07	n/a	no	96	0.49	133.24	n/a	yes
40	0.45	-2.83	n/a	?	97	0.43	0.87	n/a	yes
41	0.66	-9	n/a	yes	98	1.17	68.48	n/a	yes
42	1.64	3.16	n/a	yes	99	0.64	157.15	n/a	no
43	1.58	3.24	n/a	yes	100	0.51	-13.87	n/a	yes
44	1.31	0.1	n/a	yes	101	0.55	155.8	n/a	yes
45	0.8	0.89	n/a	yes	102	0.49	99.73	33.05	yes
46	0.59	6.04	n/a	no	103	1.48	118.12	n/a	yes
47	0.8	0.38	n/a	yes	104	0.55	10.06	n/a	?
48	2.38	2.73	n/a	no	105	0.6	5.32	n/a	?
49	0.74	-1.31	n/a	yes	106	0.7	51.65	n/a	yes
50	0.64	2.33	n/a	no	107	0.74	155.7	n/a	yes
51	0.8	50.49	n/a	yes	108	0.43	-0.74	n/a	?
52	0.66	1.11	n/a	no	109	1.13	123.92	n/a	?
53	1.77	143.05	n/a	?	110	1.27	-17.27	n/a	?
54	0.43	128.52	n/a	?	111	0.53	81.07	26.76	yes
55	1.27	-2.34	n/a	no	112	0.99	97.78	19.72	yes
56	0.66	-3.61	n/a	no	113	4.09	-0.84	n/a	no
57	0.6	82.23	7.24	no	114	4.7	102.4	28.87	yes

* TID: Target Identification; TT: Tracked Time [s]; MD: Moving direction [°] with respect to azimuth direction; MV: velocity [m/s] for targets moving within 15° of cross-track direction; R?: visually identified as real vehicle.

TABLE 2
PERFORMANCE OF THE ALGORITHM

		(VISUAL) GROUND TRUTH		
		Moving Target (MT)	Possibly (?)	False detection (FD)
ALGORITHM	Detected	63	20	31
	Not detected	25	-----	-----

TABLE 3
CLASSIFICATION AND FALSE ALARM RATE OF THE ALGORITHM

	(MT + ?) vs. FD	MT vs. (FD + ?)	MT vs. FD
Classification Accuracy	76.9%	71.6%	71.6%
False Alarm Rate	27.2%	44.7%	33.0%

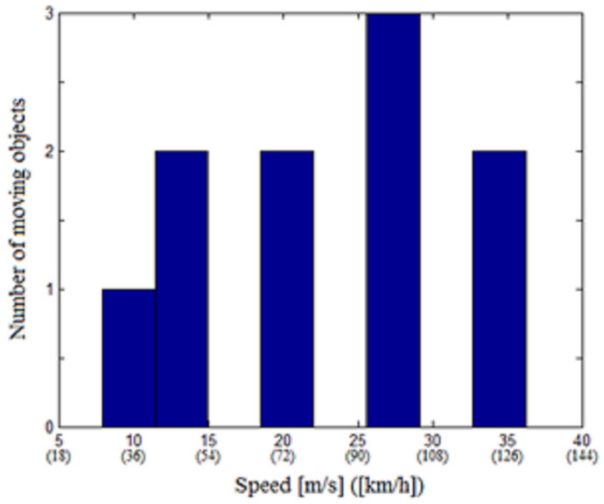

(a) Distribution of speeds for moving objects with cross-range moving direction (comparable with real 3D velocity) from Table 1.

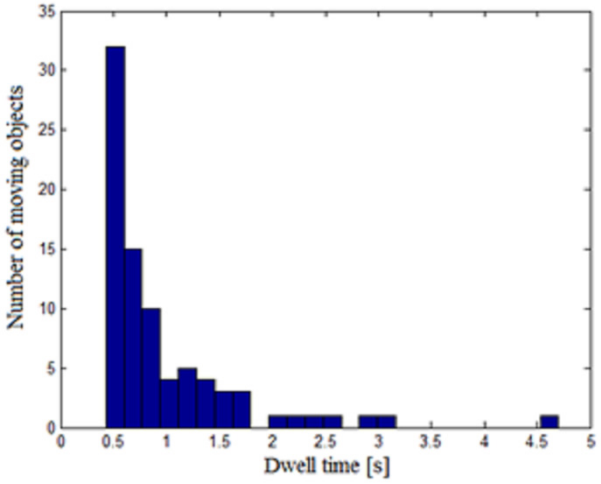

(b) Distribution of the dwell time for moving objects from Table 1.

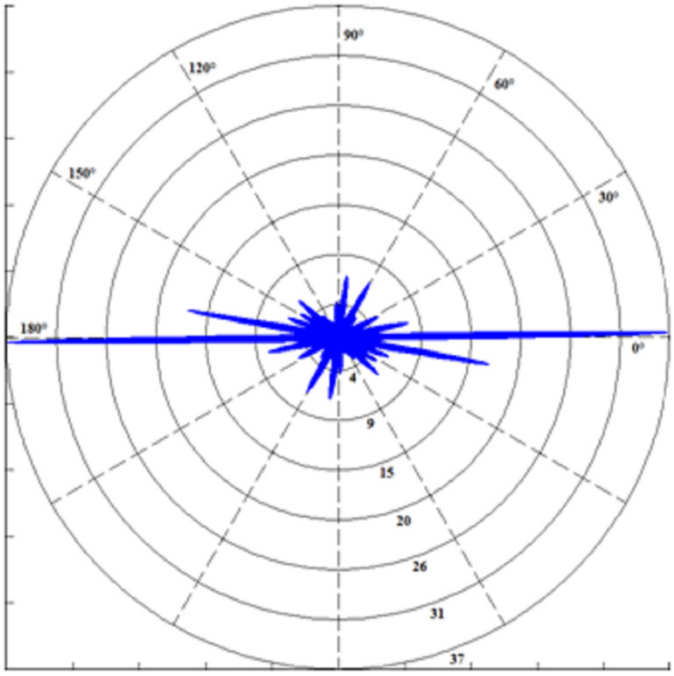

(c) Distribution of the direction of movement for moving objects from Table 1. Note the large along-track accumulation coincident with the highway.

Fig. 7. Distributions of moving objects' characteristics derived from Table 1.

A further way of evaluating the results is by using road models to overcome the problem of the sensitivity of the Doppler shift. We did this for the trajectory of target 114 by projecting the movement of the vehicle onto the south-north running highway. By inverting Eq. (8.1), we obtain an average radial velocity of 30.89m/s (varying between 30.83 and 31.02) assuming the most probable Doppler ambiguity. That is almost identical to the averaged values for platform speed, azimuth shift and range:

$$V_{radial} = -\frac{\Delta azimuth * V_{platform}}{|\overline{Range}|} \approx -\frac{143m * 34.43m/s}{1272m} \approx -3.87m/s. \quad (8.2)$$

Due to the Doppler ambiguity, it holds that

$$V_{radial}^{DopplerAmbiguity} = V_{radial} + n * 8.69m/s \quad (8.3)$$

and thus the most probable radial velocity of the vehicle on the highway is 30.89 m/s (with n=4). Below, we compare the cross-range component of the estimated speed

$$V_{cross-range}^{estimated} = \sin(102.4°) * 28.87m/s \approx 28.20m/s \quad (8.4)$$
(for values see Table 1)

with the cross-range component of the calculated radial velocity:

$$V_{cross-range}^{Doppler\ shift} = \sin(71.35°) * 30.89m/s \approx 29.27m/s \quad (8.5)$$
(with an average incidence angle of 71.35°)

obtaining a difference of only 1.07 m/s. The consistency between model and observation is highly encouraging.

IV. Conclusion & Outlook

We have introduced a tracking method based on multitarget unscented Kalman filters to not only identify moving targets but also estimate their trajectories in radar image space. The proposed algorithm can be practically applied to any single-channel, wide-beam SAR and shows promising results. For cross-range velocities, it was possible to manually validate the velocity with the help of a road model: the speed estimation was within an error margin of ~1 m/s. A more complete validation is impaired by the lack of ground truth data. A further flight campaign with a different sensor is in progress, where ground truth measurements *are* available, which will be used in a more complete validation process. In the newer campaign, along-track interferometric (ATI) data were recorded in parallel, which will provide the opportunity to compare the method developed here with ATI-based approaches. The OAwrB image processing and tracking is computationally intensive, but with high-performance computers and a trade-off in the ratio of the overlap of OAwrB images and minimum detection probability, a quasi real time processing of the data is achievable. A remaining task not addressed in this paper is the translation of an object's position and velocity in the image space to its corresponding real world position/velocity. Existing works in this field (e.g. [36]) can be incorporated to our algorithm in the future. However, as the sensor operates at high frequencies and the navigation data are not based on dGPS measurements, these corrections induce additional uncertainties and thus might not be desirable for some applications. Generally, the image to 3D correction can be done either by including the Doppler shift in the transformation function (Eq. (6.4.)), by post-processing, or by introducing additional prior information. The first solution implies additional parameters in the tracking model and consequently a less robust detection capability. The second approach for the image to 3D corrections has the advantage that it has no negative influence on the detection accuracy, but its estimation of the 3D position and velocity is less accurate and, in some cases, needs manual intervention to resolve Doppler ambiguities. The most precise method to transform image space estimates of moving targets into 3D space is by using additional prior information, most suitably road models. This allows a robust solution for the corrections even with high frequency sensors. As the main output of the paper, we were able to demonstrate with real data a novel method for tracking moving objects in single-channel wide-beam SAR systems with high accuracy in the image space and flexibility concerning the sensor and object moving directions (cross-track as well as along-track) and speeds.

Acknowledgement

The authors would like to thank the MiSAR team at EADS for their cooperation and for providing the raw data for the experiments, the anonymous reviewers for their valuable comments that improved this paper and armasuisse W+T for funding the work. This work was conducted at the Remote Sensing Laboratories, University of Zurich, Zurich, Switzerland.

References

[1] P. M. Corbell, J. J. Perez and M. Rangaswamy, "Enhancing GMTI Performance in Non-Stationary Clutter Using 3D STAP," in *IEEE Radar Conference 2007*, pp. 647-652, 2007.

[2] Z. Zhang, W. Xie, W. Hu and W. Yu, "Local Degrees of Freedom of Airborne Array Radar Clutter for STAP," *IEEE Geoscience and Remote Sensing Letters*, vol. 6, pp. 97-101, 2009.

[3] A. Budillon, V. Pascazio and G. Schirinzi, "Estimation of Radial Velocity of Moving Targets by Along-Track Interferometric SAR Systems," *IEEE Geoscience and Remote Sensing Letters,* vol. 5, pp. 349-353, 2008.

[4] E. Chapin and C. W. Chen, "Along-track interferometry for ground moving target indication," *IEEE Aerospace and Electronic Systems Magazine,* vol. 23, pp. 19-24, 2008.

[5] W. Genyuan, X. Xiang-Gen, V. C. Chen and R. L. Fielder, "Detection, location, and imaging of fast moving targets using multifrequency antenna array SAR," *IEEE Transactions on Aerospace and Electronic Systems,* vol. 40, pp. 345-355, 2004.

[6] M. I. Pettersson, "Optimum relative speed discretisation for detection of moving objects in wide band SAR," *IET Radar, Sonar and Navigation,* vol. 1, pp. 213-220, 2007.

[7] M. Rüegg, E. Meier and D. Nüesch, "Capabilities of Dual-Frequency Millimeter Wave SAR with Monopulse Processing for Ground Moving Target Indication," *IEEE Transactions on Geoscience and Remote Sensing*, vol. 45, pp. 539-553, 2007.

[8] J. R.Fienup, "Detecting moving targets in SAR imagery by focusing," *IEEE Transactions on Aerospace and Electronic Systems*,vol. 37, pp. 794-809, 2001.

[9] S. Suchandt, H. Runge, H. Breit, U. Steinbrecher, A. Kotenkov and U. Balss, "Automatic Extraction of Traffic Flows Using TerraSAR-X Along-Track Interferometry," *IEEE Transactions on Geoscience and Remote Sensing*, vol. 48, pp. 807-819, 2010.

[10] C. H. Gierull, "Ground moving target parameter estimation for two-channel SAR," in *IEE Proceedings on Radar, Sonar and Navigation*, vol. 153, pp. 224-233, 2006.

[11] A. R. Brenner and J. H. G. Ender, "Demonstration of advanced reconnaissance techniques with the airborne SAR/GMTI sensor PAMIR," in *IEE Proceedings on Radar, Sonar and Navigation,* vol. 153, pp. 152-162, 2006.

[12] D. Cerutti-Maori, J. Klare, A. R. Brenner and J. H. G. Ender, "Wide-Area Traffic Monitoring With the SAR/GMTI System PAMIR," *IEEE Transactions on Geoscience and Remote Sensing*, vol. 46, pp. 3019-3030, 2008.

[13] D. Cerutti-Maori, C. H. Gierull and J. H. G. Ender, "Experimental Verification of SAR-GMTI Improvement Through Antenna Switching," *IEEE Transactions on Geoscience and Remote Sensing*, vol. 48, pp. 2066-2075, 2010.

[14] M. Edrich and G. Weiss, "Second-generation Ka-Band UAV SAR System," in *European Radar Conference, EuRAD 2008*, pp. 479-482, 2008.

[15] M. Edrich, "Ultra-lightweight synthetic aperture radar based on a 35 GHz FMCW sensor concept and online raw data transmission," in *IEE Proceedings on Radar, Sonar and Navigation*, vol. 153, pp. 129-134, 2006.

[16] Y. Bar-Shalom, F. Daum and J. Huang, "The probabilistic data association filter," *IEEE Control Systems*, vol. 29, pp. 82-100, 2009.

[17] Z. Khan, "MCMC-Based Particle Filtering for Tracking a Variable Number of Interacting Targets," *IEEE Transactions on Pattern Analysis and. Machine Intelligence,* vol. 27, pp. 1805-1918, 2005.

[18] F. Pei, P. Cui and Y. Chen, "Adaptive MCMC Particle Filter for Nonlinear and Non-Gaussian State Estimation," in *Proceedings of the 2008 3rd International Conference on Innovative Computing Information and Control,* 2008.

[19] L. Scharenbroich, G. Magnusdottir, P. Smyth, H. Stern and C.-C. Wang, "A Bayesian framework for storm tracking using a hidden-state representation," *Monthly Weather Review,* vol. 138, pp. 2132–2148, 2009.

[20] D. Henke, A.Barmettler, E. Meier and M. E. Schaepman, "Moving target tracking in multistatic low-frequency UWB SAR data - Theory and simulated results," Remote Sensing Laboratories, University of Zurich, report to armasuisse, ARAMIS-Nr. R-3210/040-15, pp 65-94, 2010.

[21] I. G. Cumming and F. H. Wong, *Digital Processing of Synthetic Aperture Radar Data, Algorithms and Implementation*. Artech House, Boston, 2005.

[22] J. C. Curlander and R. N. McDonough, *Synthetic Aperture Radar - Systems and Signal Processing*, John Wiley & Sons, New York, 1991, pp. 440-443.
[23] C. Magnard, M. Frioud and E. Meier, "Processing, geocoding and mosaicking of MiSAR data," in *Proceedings of ISPRS 3-Ländertagung DGPF - OVG - SGPBF,* pp. 524-531, 2010.
[24] R. Lanari, S. Hensley and P. Rosen, "Modified SPECAN algorithm for ScanSAR data processing," in *Proceedings of IEEE International Symposium on Geoscience and Remote Sensing, IGARSS 1998*, vol. 2, pp. 636-638, 1998.
[25] E. Meier, U. Frei and D. Nüesch, "Precise Terrain Corrected Geocoded Images," in Schreier G. (ed.) *SAR Geocoding: Data and System*. Wichmann, 1993, pp. 173-186.
[26] K. Robinson and P. F. Whelan, "Efficient morphological reconstruction: a downhill filter," *Pattern Recognition Letters*, vol. 25, pp. 1759-1767, 2004.
[27] R. Klette and A. Rosenfeld, *Digital Geometry—Geometric Methods for Digital Picture Analysis.* Morgan Kaufmann, 2004.
[28] Y. Bar-Shalom, P. K. Willett, and X. Tian, *Tracking and Data Fusion: A Handbook of Algorithms*. YBS Publishing, 2011.
[29] E. A. Wan and R. Van Der Merwe, "The unscented Kalman filter for nonlinear estimation," in *Proceedings of IEEE Adaptive Systems for Signal Processing, Communications, and Control Symposium, AS-SPCC 2000*, pp. 153-158, 2000.
[30] D. G. Khairnar, S. N. Merchant and U. B. Desai, "Nonlinear Target Identification and Tracking Using UKF," in *Proceedings of IEEE International Conference on Granular Computing*, 2007.
[31] A. Doucet, N. de Freitas, and N. Gordon, editors. *Sequential Monte Carlo Methods in Practice*. Springer, 2001.
[32] S. Särkkä, A. Vehtari and J. Lampinen, "Rao-Blackwellized particle filter for multiple target tracking," *Information Fusion,* vol. 8, pp. 2-15, 2007.
[33] S. Särkkä, A. Vehtari and J. Lampinen, "Rao-Blackwellized Monte Carlo data association for multiple target tracking," in *Proceedings of the International Conference on Information Fusion*, pp. 583-590, 2004.
[34] S. J. Julier, "The scaled unscented transformation," in *Proceedings of the American Control Conference 2002*, vol. 6, pp. 4555-4559, 2002.
[35] S. J. Julier and J. K. Uhlmann, "Unscented filtering and nonlinear estimation," *Proceedings of the IEEE*, vol. 92, pp. 401-422, 2004.
[36] M. Kirscht, "Detection and imaging of arbitrarily moving targets with single-channel SAR," in *IEE Proceedings on Radar, Sonar and Navigation*, vol. 150, pp. 7-11, 2003.

Daniel Henke received his Dipl.-Inf. degree in computer science at the Albert–Ludwigs University, Freiburg, Germany, in 2007. He has been working toward his Ph.D. at the University of Zürich, Zürich, Switzerland, since the beginning of 2009.
He worked as Junior Specialist on a project involving cloud tracking in optical remote sensing at the Earth System Science Department, School of Physics at the University of California, Irvine, USA. He is currently a Research Assistant with the Remote Sensing Laboratories, University of Zürich. His research interests include detecting and tracking techniques for moving objects in remote sensing applications, probabilistic modeling, and signal processing.

Christophe Magnard received the M. Sc. in microengineering from the Swiss Federal Institute of Technology (EPFL), Lausanne, Switzerland in 2005. He has been working toward his Ph.D. at the University of Zürich, Zürich, Switzerland, since the beginning of 2006.
He is employed as a Research Assistant at the Remote Sensing Laboratories, University of Zurich. His research interests include SAR focusing algorithms, geocoding of SAR data, multi-baseline SAR interferometry with millimeter-wave radar and other SAR-related techniques.

Max Frioud received his degree in theoretical physics from the University of Fribourg, Switzerland in 1992 and a Ph.D. degree from the University of Neuchâtel, Switzerland in 2003.
He worked as a Ph.D. from 1997 to 2003 in the Lidar group from the Observatory of Neuchâtel, where he was mainly involved in the processing of aerosol backscatter lidar data, and wrote a thesis intitulated "Application of backscatter Lidar to determine the aerosol distribution above complex terrain". In 2004 he was awarded a Marie-Curie mobility research training grant and worked from 2005 to 2007 as a post-doc at the Arctic Lidar Observatory for Middle Atmosphere Research in Andenes, Norway, where he was mainly involved in the hardware development and in the quality assurance of a new troposphere lidar.
He joined the Remote Sensing Laboratories in 2007 as a research associate. He has been working since then on the development of SAR data processors, especially in the quality assurance of a Modular SAR Processor. His current focus of interest is the processing of FMCW SAR data from UAV platforms.

David Small (S'85–M'98) was born in Ontario, Canada. He received the B.A.Sc. degree in systems design engineering from the University of Waterloo, Waterloo, ON, Canada, in 1988, the M.A.Sc. degree in electrical engineering from the University of British Columbia (UBC), Vancouver, BC, Canada, in 1991, and the Ph.D. degree from the University of Zürich (UZH), Zürich, Switzerland, in 1998.
He is currently a Senior Research Scientist and Co-Leader of the SAR group within the Remote Sensing Laboratories of the University of Zürich. In the past, he has researched improvements to generation of height models using cross-track radar interferometry, and geometric calibration and validation for a variety of SAR sensors. He is presently researching the extension of radar image simulation software to incorporate further mode-specific parameterizations and monitor systematic signatures of snow melt over large areas. He is a member of the European Space Agency's Quality Working Group for SAR sensors.
Dr. Small is a member of the IEEE-GRS Society. He was chair of the CEOS SAR calibration/validation workshop in 2010.

Erich Meier received the M.Sc. degree in geography and the Ph.D. (Hons.) degree in remote sensing from the University of Zürich, Zürich, Switzerland, in 1982 and 1989, respectively.
From 1979 to 1982, he was a Research Assistant with the Remote Sensing Section, and from 1982 to 1983, he was with the GIS Laboratory, Department of Geography, University of Zürich. From 1983 to 2006, he was a Research Scientist with the Remote Sensing Laboratories (RSL), University of Zürich, where he is currently a Research Section Head who is involved in teaching as well as in research in digital image processing, and radiometric and geometric calibration of SAR data. Since 2000, he has been the Head of the SARLab, a research group within RSL. The main research interests of this group include the development of new focusing algorithms for SAR data from UHF to millimeter wave, interferometry, polarimetry, and MTI algorithms as well as calibration and validation activities for spaceborne and airborne systems. He is a Consultant on behalf of several national and international organizations and private companies.

Michael E. Schaepman (M'05-SM'07) holds a MSc (1993) and Ph.D. degree (1998) in Geography from the University of Zurich (CH). In 1999, he spent his PostDoc time at the Optical Science Center of the University of Arizona (Tucson, USA). In 2000, he was appointed project manager of the ESA APEX (Airborne Prism Experiment) spectrometer. In 2003, he accepted a position as full chair of geo-information science and remote sensing at Wageningen University (Wageningen, NL). In 2009 he was appointed full chair of remote sensing at the University of Zurich (CH). He is currently heading the Remote Sensing Laboratories at this University. His interests are in the computational Earth sciences using remote sensing and physical models, with particular focus on the land-atmosphere interface using imaging spectroscopy.